crystals

MDPI

Article

A Study on Apatite from Mesozoic Alkaline Intrusive Complexes, Central High Atlas, Morocco

Pengyu Yuan, Bo Xu *, Zixuan Wang and Daiyue Liu

School of Gemmology, China University of Geoscience Beijing, 29 Xueyuan Road, Haidian District, Beijing 100086, China; yuanpengyu@cugb.edu.cn (P.Y.); zane.wzx@foxmail.com (Z.W.); 18822303435@163.com (D.L.)

* Correspondence: bo.xu@cugb.edu.cn

Abstract: There are abundant phosphate mines in the High Atlas Mountains of Morocco. Gem-quality apatite is produced at the Anemzi deposit, but its associated gem mineralogy is relatively poorly studied. In this study, apatite from the Anemzi mine in Morocco was analysed using standard gemmological characterisation methods, including basic tests (hardness, relative density, microscopy, etc.), spectroscopic tests (infrared, Raman, and ultraviolet–visible spectroscopy), and chemical analyses (electron probe and laser ablation inductively coupled plasma mass spectrometry). This paper explores the gemmological characteristics of Moroccan apatites and the information on diagenesis recorded for apatites by comparing them with apatites from other sources. Apatite from the Anemzi deposit is an igneous fluorapatite. The relatively high Cl content of the apatite suggests that the magma in the area has a high Cl content, whereas the high Cl/F ratio may indicate that the deposit formed in a slab subduction environment. The characteristics of the major and trace elements indicate high oxygen and sulphur escapes in the apatite-forming magma.

Keywords: apatite; halogen elements; Raman spectroscopy; magmatic oxidation; LA-ICP-MS

check for updates

Citation: Yuan, P.; Xu, B.; Wang, Z.; Liu, D. A Study on Apatite from Mesozoic Alkaline Intrusive Complexes, Central High Atlas, Morocco. *Crystals* **2022**, *12*, 461. https://doi.org/10.3390/cryst12040461

Academic Editors: Taijin Lu, Fei Liu, Tingting Gu and Francesco Capitelli

Received: 18 February 2022
Accepted: 19 March 2022
Published: 25 March 2022

Publisher's Note: MDPI stays neutral with regard to jurisdictional claims in published maps and institutional affiliations.

Copyright: © 2022 by the authors. Licensee MDPI, Basel, Switzerland. This article is an open access article distributed under the terms and conditions of the Creative Commons Attribution (CC BY) license (https://creativecommons.org/licenses/by/4.0/).

1. Introduction

Apatite is a common phosphate mineral with an extremely wide distribution in the Earth's crust, occurring in sedimentary, igneous, and metamorphic rocks [1–3]. Apatite is one of the major indicator minerals for petrogenesis, magmatic differentiation progression, and diagenetic conditions because it is rich in trace and rare earth elements, which saves and records information about the source magma [4,5]. At the same time, due to the lattice flaws caused by the internal homogeneous substitution of its analogues, apatite is a significant gemstone mineral with a variety of colours.

In the world resources, the output of phosphate is dominated by sedimentary phosphate masses, and the output of pyrogenic phosphate rock only accounts for 10% of the total production. Morocco is the main holder and producer of sedimentary phosphate block rock, whereas there is igneous phosphate block rock output in the High Atlas Mountains. Pyrogenic apatite not only provides high-quality phosphate concentrates, but also contains low levels of deleterious substances and is rich in rare earth elements [6].

The optimal chemical formulation of apatite is $X_5(ZO_4)_3Y$, where site X is primarily occupied by Ca^{2+}; site Z is taken up by P^{5+}; and site Y is occupied by F^-, Cl^-, and OH^- [7].

The most common phase in the rocks is fluorapatite ($Ca_5[PO_4]_3F$) [8]. Fluorapatite ($Ca_5[PO_4]_3F$) is composed of hexagonal crystals tightly packed with tetrahedral PO_4^{3-} groups, forming two channels that are parallel to the hexagonal axis. In this structure, Ca has two sub-positions, namely, Ca1 and Ca2. Forty percent of Ca occupies the small channel of the ninefold collocation (Ca1), whereas F dominates the central part of the large channel. Sixty percent of Ca forms sevenfold coordination (Ca2) around F in a larger channel. This structure can tolerate relatively large structural distortions and allow different substitutions [9]. Of all the trace elements in fluorapatite, Na^+, Eu^{2+}, Fe^{2+}, Mg^{2+}, Pb^{2+}, Mn^{2+}, Sr^{2+},

REE^{3+}, U^{4+}, and Th^{4+} preferentially access the X site, whereas the Z site tends to be occupied by Si^{4+}, S^{6+}, and C^{4+}. The monovalent ion Na^{+} is the common minor component and is usually located at the Ca1 site. The monovalent ion Na^{+} can access the fluorapatite through the following three substitutions (V stands for vacancy) [10,11]: $REE^{3+} + Na^{+} = 2Ca^{2+}$; $Na^{+} + S^{6+} = Ca^{2+} + P^{5+}$; $2Na^{+} = Ca^{2+}$+ [V]. On the basis of the charge conservation principle, the addition of monovalent ions involves the existence of alternative ionic groups, such as REE^{3+} or SO_4^{2-}. REE^{3+} and Y^{3+} can occur in higher concentrations and occupy the Ca2 site, whereas SO_4^{2-} occupies the PO_4^{3-} site. Possible alternative reactions for REE^{3+} and Y^{3+} include [12–14]: $REE^{3+} + SiO_4^{4-} = Ca^{2+} + PO_4^{3-}$; $REE^{3+} + O^{2-} = Ca^{2+} + F^{-}$. Divalent ions can be doped into apatite at different concentrations because they have a common charge and a similar cation size as Ca^{2+}. The most abundant tetravalent ions (Th^{4+} and U^{4+}) in natural apatite can enter the apatite by the following complex substitution (V represents vacancy) [9,15–17]: $Th^{4+}(U^{4+}) + [V] = 2Ca^{2+}$. The PO_4^{3-} ion cluster can be substituted by the AsO_4^{3-}, SO_4^{2-}, CO_3^{2-}, and SiO_4^{4-} ion clusters [18–21]. For valence equilibrium (SO_4^{2-} as an example), the following substitutions can occur [19]: $SO_4^{2-} + SiO_4^{4-} = 2PO_4^{3-}$; $SO_4^{2-} + Na^{+} = PO_4^{3-} + Ca^{2+}$.

In this study, gem-quality apatite crystals from the Anemzi deposit in Morocco were selected, and gemmological, spectroscopy, and major and trace element analyses were performed to determine the gemmological characteristics and mineralisation environment of these crystals. This study helps to further supplement the development of apatite resources in Morocco. Since there are few relevant studies on apatite in Morocco, the advantages of this study are as follows: (1) the gemmological and mineralogical studies on apatite can be theoretically enriched, and (2) Morocco is established as an important producer of apatite, having abundant phosphorite resources. The results of this study will support the theory of apatite mineralisation in the region.

2. Geological Setting

The Atlas Mountains, a series of mountain ranges in north-western Africa, are the most extensive folded and fractured mountain region in Africa, being part of the Alpine system. The Grand Atlas Mountains (Middle Atlas, High Atlas, and Anti-Atlas) are located in Morocco and are an important phosphate extraction area yielding gem-grade apatite (Figure 1a).

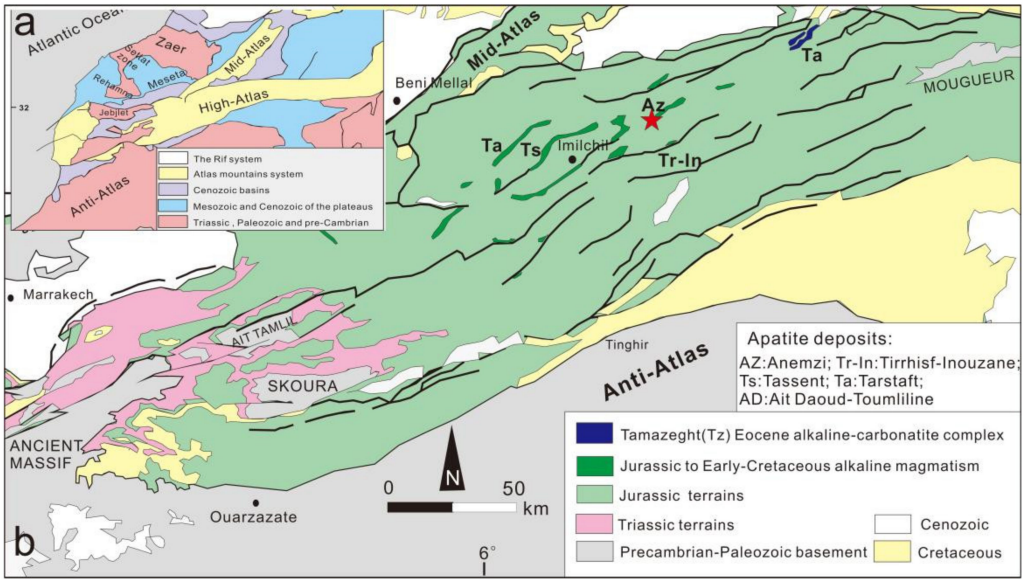

Figure 1. (**a**) Map of the Atlas Mountains in Morocco (the dashed box marks the study area in this paper). (**b**) Geological map of the High Atlas Mountains, with the samples marked with a red star. Modified from [6] and the references within it.

The geology of the Middle Atlas is distinguished by two west–east trending Palaeozoic rock outcrops, namely, the Rehamna area and the Zaer Massif, which are separated by Settat, a marine sediment area from Upper Cretaceous to Eocene. Palaeozoic rocks are usually Hercynian schist, and granite, monzonitic granite, and monzonite to monzodiorite intrude and make contact with the metamorphic parts of Hercynian schist [22–24]. The Anti-Atlas is the thick-skinned Palaeozoic folded belt, and its Precambrian basement appears in several inverted chimeras or 'boutonnieres' [23,25]. These chimeras include Paleoproterozoic and Early–Middle Neoproterozoic rocks influenced by the Pan-African Fault about 660 Ma ago [23].

The High Atlas (up to 4000 m above sea level) is a representative intracontinental Alpine orogeny which forms a retrograde chain of converging the Afro-Eurasian continents. Its growth began in the early Mesozoic, and the Pangu fault reactivated, forming a subsidence basin, leading to the Atlantic Ocean opening on the edge of northwest Africa [6,26–30]. This mountain chain includes the Eastern, Western, and Central High Atlas. Compared to the eastern and western sections, the Central High Atlas is located in the deepest part of the orogenic belt. Furthermore, the heart of the Central High Atlas dorsal–slope ridge was formed by a significant Jurassic–Cretaceous alkaline-to-transitional magmatism that occurred between about 165 and 125 Ma ago (Figure 2b) [6,27,31]. The main apatite deposits in the high latitudes of central Morocco, including the Anemzi, Tasraft, Ait Daoud–Toumliline, Tirrhist–Inouzane, and Tassent deposits, are always correlated in space with these Jurassic–Cretaceous alkaline intrusions (Figure 2b) [29,32]. Further gemmological and mineralogical studies on apatite from Anemzi, Morocco, are presented in this paper.

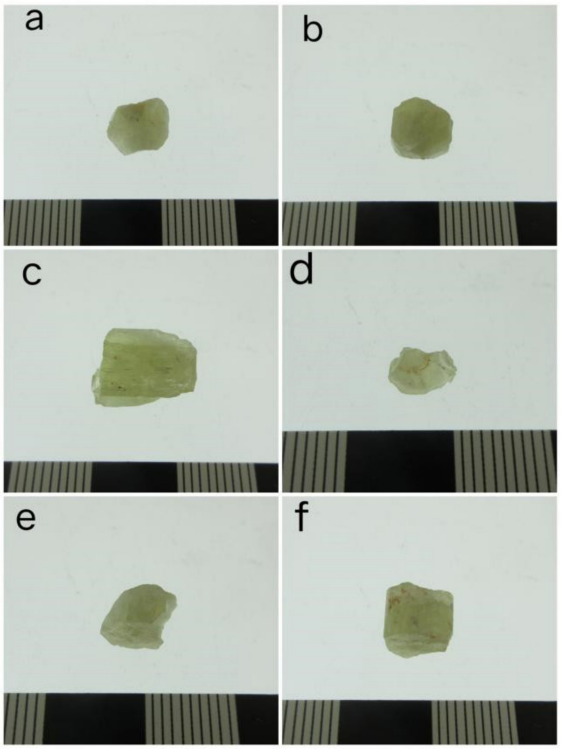

Figure 2. (**a**–**f**) Apatite crystals Moro-1 to Moro-6 from Morocco.

3. Materials and Methods

Standard gemmological tests were performed on six apatites (Moro-1 to Moro-6) from the Anemzi deposit in Morocco.

The gemmological tests of the sample base were performed at the Gemmological Research Laboratory of the China University of Geosciences (Beijing), including optical features, ultraviolet (UV) fluorescence, and gemmological microscopic features. The refrac-

tive index and birefringence were measured with a refractometer on a selected polished and flat surface of apatite, and diiodomethane was used as the refractive oil. The specific gravity of the samples was measured using a hydrostatic weighing method. Fluorescence was observed with UV fluorescent lamps at wavelengths of 365 and 254 nm.

The infrared spectra were tested using a Tensor 27 Fourier-transform infrared spectrometer (Bruker, Billerica, Germany) and a reflection method. The reflection method conditions were as follows: scanning temperature of 18–25 °C, humidity of less than 70%, scanning voltage of 85–265 V, resolution of 4 cm^{-1}, grating of 6 mm, test range of 400–2000 cm^{-1}, and scanning signal accumulation of 32 times.

An HR-Evolution-type micro-Raman spectrometer (HORIBA, Shimadzu, Japan) was used to perform Raman spectroscopy tests at 532 nm. The Raman spectroscopy test conditions were as follows: scanning range of 400–4000 cm^{-1}, laser power of 50 mW, resolution of 4 cm^{-1}, slit width of 100 μm, grating of 600 gr/mm, scanning time of 4 s, and integration time of 3 s.

The UV–visible (UV–VIS) spectroscopy test used a UV-3600 UV–VIS spectrophotometer (Shimadzu Corporation, Kyoto, Japan) to measure the absorption value using a transmission method. The transmission method conditions were as follows: wavelength of 300–800 nm, slit width of 20 nm, time constant of 1.0 s, medium scanning speed, and sampling interval of 0.5 s.

In this experiment, Moro-1 and Moro-2 were selected as samples. To obtain a more representative elemental content, a homogeneous portion of the apatite samples without inclusions was selected for testing.

The apatite crystals were first mechanically crushed, after which the internally pure part of the sample was selected under a binocular microscope and placed in an epoxy block to polish it to the largest surface. The polished portions were surface carbon blasted before testing. The primary elements were tested at Macquarie University in Australia using a JXA-8230 electron probe microanalyser. The test conditions were as follows: accelerating voltage of 15.0 kV, electron beam current of 2×10^{-8} A, and beam spot of 5 μm. The test accuracy of each element was greater than 0.001% and corrected using the ZAF correction method.

At the Institute of Geomechanics, Chinese Academy of Geological Sciences, a laser ablation inductively coupled plasma mass spectrometer was used to measure the trace element composition of the samples. A 193 nm excimer laser ablation system (GeoLas HD; Coherent, Santa Clara, CA, USA) and a four-stage rod mass spectrometer (Agilent 7900) were used for inline testing, with Ar and He as the carrier gases. For measuring the trace element content, this study mainly used NIST SRM 610 and 612 as external standards and ^{43}Ca as an internal standard for trace amounts.

4. Results

4.1. Visual Appearance and Gemmological Properties of Apatite

The tested apatites (Moro-1 to Moro-6) were yellowish green with a glassy to weak glassy lustre. Because of the large number of internal fissures in the samples, the transparency was poor, translucent to opaque, and it was difficult to observe the internal inclusions. When observed under a bright field-of-view illumination of a gemstone microscope, longitudinal lines on the crystal surface parallel to the c-axis were visible, and brown impurity was present on the surface. The crystals were hexagonal, with shell and uneven fractures, and the fractures had a greasy lustre. The apatite sizes ranged from 7 mm to 1.4 cm, with thickness from 3 mm to 8 mm (Figure 2).

The RI of the samples was measured with a gem refractometer and ranged from 1.635 to 1.640. The specific gravity values varied between 3.18 and 3.20. All samples were inert at long wavelengths of the UV fluorescent lamps. Except for Moro-1 and Moro-2, which showed very weak pink-purple fluorescence at short wavelengths, all the other samples were inert at short wavelengths.

4.2. Spectral Characteristics

4.2.1. Infrared Spectrum

A Fourier transform infrared spectrometer was used to test the six apatites. According to the literature on apatites, the infrared spectrum vibration of apatites is mainly manifested in the vibration of $[PO_4]^{3-}$ ions. There are four fundamental frequencies of $[PO_4]^{3-}$, which are symmetric stretching vibration (v_1), bending vibration (v_2), anti-symmetric stretching vibration (v_3), and bending vibration (v_4) [33,34]. The v_1 band is a single, symmetric A, the v_2 band comes from a doubly generated vibration E, and the v_3 and v_4 bands are triple degenerate vibration F_2.

In the infrared spectra of 400–2000 cm^{-1} of the Moroccan apatites, the following characteristic peaks were found: a weak absorption peak at 966 cm^{-1}, which was caused by the symmetric stretching vibration (v_1) of $[PO_4]^{3-}$, and an absorption shoulder near 1051 cm^{-1} and a strong absorption peak at 1098 cm^{-1}, which were caused by the anti-symmetric stretching vibration (v_3) of $[PO_4]^{3-}$. The moderately strong absorption peaks at 571 cm^{-1} and 602 cm^{-1} were caused by the bending vibration (v_4) of $[PO_4]^{3-}$, and the absorption peak at 470 cm^{-1} was attributed to the v_3–v_4 difference band of $[PO_4]^{3-}$. The anti-symmetric stretching and bending vibrations, that is, respectively, v_3 and v_4 bands were divided into components, and v_1 band was active [35]. Both of these facts prove that the symmetry of the phosphate ion was lowered C_{3v} or C_3.

The fluorapatite from Cerro de Mercado mine, Mexico, whose ID was R040098 in RRUFF database, had two moderately strong v_4 bands measured at 571 cm^{-1} and 603 cm^{-1}; a sharp v_1 band was found at 966 cm^{-1}; and strong v_3 bands were measured near 1032 cm^{-1} and 1087 cm^{-1}. Comparing Moroccan samples with R040098, we found that the absorption peak at 966 cm^{-1} of samples was weaker. The v_3 vibration of $[PO_4]^{3-}$ with a significant right shift and the v_3 bands widened. The splitting of the P–O bond and the interaction of the vibration pattern of the $[PO_4]^{3-}$ tetrahedron with the crystal lattice of the fluorapatite may have been responsible for the widening of the v_3 bands [35]. In addition, by comparison, the infrared spectra of the samples were found to be consistent with fluorapatite. Therefore, it can be preliminarily judged that apatite of Moroccan origin is fluorapatite (Figure 3a).

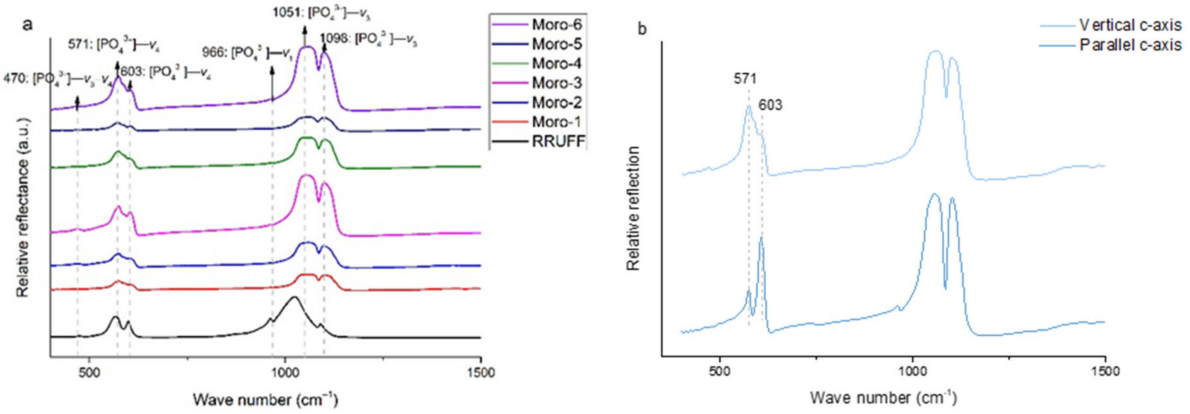

Figure 3. (**a**) Infrared spectra of the Moroccan apatites. (**b**) Infrared spectra of the Moroccan apatite at different orientations.

Furthermore, the infrared spectra of the samples were tested at different orientations of the crystal, and it was found that the apatite was axial. The infrared spectra obtained from the parallel and vertical c-axis measurements differed between 560 and 610 cm^{-1}. This difference was demonstrated by the different intensities of the $[PO_4]^{3-}$ bending vibration peak (Figure 3b). The parallel c-axis measurement results showed that the absorption peak at 603 cm^{-1} was stronger than that at 571 cm^{-1}, whereas the vertical c-axis measurement results showed the opposite.

4.2.2. Raman Spectrum

The Raman spectra of the Moroccan apatites appeared at 400–1500 cm^{-1}. The Raman characteristic peaks of the apatites were mainly reflected in the vibrations of the $[PO_4]^{3-}$ ion cluster. Symmetric stretching vibration peaks of the ion cluster can be seen at 962–965 cm^{-1}, bending vibration peaks were detected at 419–431 cm^{-1}, asymmetric stretching vibration peaks were observed at 1040–1049 cm^{-1}, and asymmetric bending vibration peaks were detected at 575–593 cm^{-1}.

By analysing and comparing the Raman spectra of the samples, the following characteristic peaks were found: a weak absorption peak at 428 cm^{-1} caused by the bending vibration of $[PO_4]^{3-}$, a medium–strong absorption peak at 587 cm^{-1} and the weak absorption peak at 606 cm^{-1} caused by the asymmetric bending vibration of $[PO_4]^{3-}$, a strong absorption peak at 962 cm^{-1} caused by the symmetric stretching vibration of $[PO_4]^{3-}$, and peaks at 1051 cm^{-1} and 1078 cm^{-1} resulting from the asymmetric stretching vibration of $[PO_4]^{3-}$ (Figure 4). When compared with the standard Raman spectrum of fluorapatite, it can be determined that the apatites from Morocco were fluorapatites.

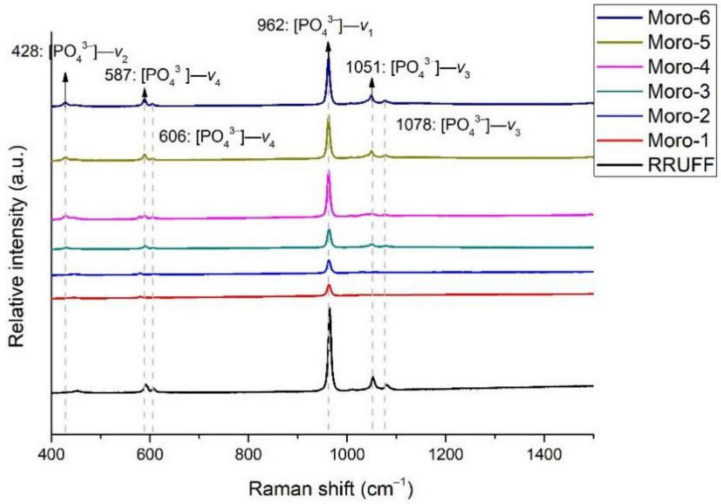

Figure 4. Raman spectra of the Moroccan apatites.

4.2.3. UV–VIS Spectrum

Apatite contains a variety of rare earth elements, which have important influence on its colour and fluorescence. Apatite with a high total REE absorbs more strongly in the UV region; the blue and orange–yellow regions also absorb more strongly than apatite with a low total REE [36]. The absorbance of the samples was measured with a UV–VIS spectrophotometer. The UV spectra of the six apatites are shown in Figure 5.

The samples had obvious absorption in the red–yellow region with a distinct peak between 450 and 750 nm. In addition, the moderately narrow band peaks at 450–750 nm can be attributed to Pr^{3+} near 450 nm and the energy level transition (4f–5d) of Nd^{3+} at 530 nm, 580 nm, and 748 nm [37–39]. In addition, the samples showed a greenish tone, which was related to the combined absorption of the orange–red and violet regions [36]. Moro-3, Moro-4, and Moro-6 showed strong absorption peaks near 370 nm, which were caused by the charge transfer transition of Ce^{3+}/Ce^{4+} [37]. However, the difference in UV spectra between the samples may reflect differences in content of rare earth elements or the different orientation of the tested samples.

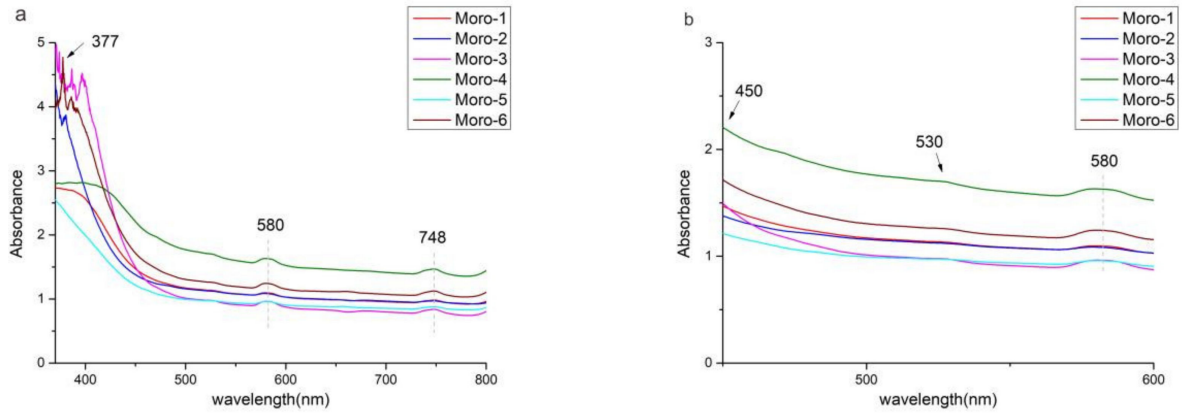

(**a**) (**b**)

Figure 5. UV–VIS spectra of the Moroccan apatites. (**a**) From 360 nm to 800 nm. (**b**) From 450 nm to 600 nm.

4.3. Major and Trace Elements

The major and trace elements of Moro-1 and Moro-2 are shown in Tables 1 and 2. On the basis of the results of the tests and calculations, the main chemical components of Moroccan apatites were CaO and P_2O_5, which were found in the following proportions: CaO = 53.98–54.55 wt % and P_2O_5 = 39.47–40.59 wt %. The results were consistent with the compositional range of pyrogenic apatite (CaO = 54–57 wt % and P_2O_5 = 39–44 wt %) described by Belousova [3]. Due to the small difference in the EPMA measurements, this study selected a point to calculate separately the crystal chemical formulae of Moro-1 and Moro-2. It was found that the chemical formula of Moro-1 was $(Ca_{4.77}, Ce_{0.01}, Sr_{0.003}, Fe_{0.001}, Na_{0.01})_{4.81}[(P_{2.77}, S_{0.03}, Si_{0.04})_{2.93}O_{12}](F_{0.13}, Cl_{0.07}, OH_{0.05})_{1.0}$. On the other hand, the chemical formula of Moro-2 was $(Ca_{4.71}, Ce_{0.01}, Sr_{0.003}, Fe_{0.001}, Na_{0.01})_{4.81}[(P_{2.77}, S_{0.03}, Si_{0.05})_{2.939}O_{12}](F_{0.16}, Cl_{0.09}, OH_{0.06})_{1.0}$, which is that of fluorapatite.

The abundance of the apatite trace elements given in Table 3 indicate that the apatites contained a variety of trace elements. The most extensive trace elements in the Moroccan apatites were rare earth elements (La, Nd, and Ce), Sr, Th, U, Mn, etc. The samples contained 610.33–650.80 ppm of Sr, 86.76–107.82 ppm of Mn, 1.60–1.81 ppm of Pb, 181.57–204.33 ppm of Th, and 16.24–18.91 ppm of U. The total rare earth element content of the Moroccan apatite was 6031.54–6544.27 ppm, and the total LREE content was 5819.89–6307.31 ppm. The analytical results showed that in the chondrite standardisation model (Figure 6), the samples displayed a right-skewed distribution, wherein light rare earth elements were slightly enriched and heavy rare earth elements were relatively deficient. The range of δEu was 0.53–0.59, showing a weak negative Eu anomaly; δCe ranged from 1.00 to 1.08 with no obvious Ce anomaly.

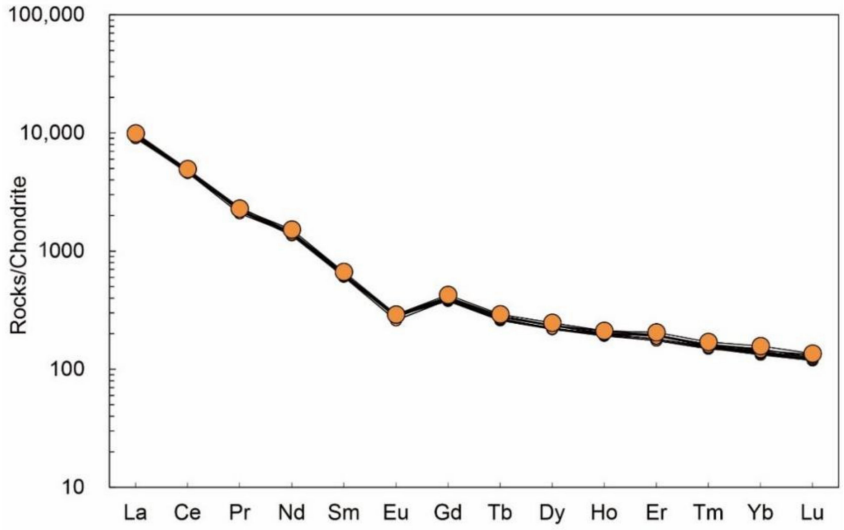

Figure 6. Chondrite-normalised REE distribution patterns of Moroccan apatites. The normalisation values for chondrite were from McDonough and Sun (1989) [40].

5. Discussion

5.1. Gemmological Characteristics

The test results were compared with the existing data for apatite from other origins (Table 4), which indicated that the optical and physical properties of the apatite from Morocco are almost the same as those of apatites from all other locations. The colour of the Moroccan apatite is yellowish green, which is similar to the apatite produced in Mexico. However, most Moroccan apatites have low transparency and many cracks. Compared with the apatites from other places, the Moroccan apatite has a slightly larger RI.

5.2. Major and Trace Elements

5.2.1. Halogen Element Characteristics of Apatite

Yang's [41] paper studied apatites from nine origins, namely AP and MAD from Madagascar, Durango from Mexico, Otter Lake from Canada, NW–1 fron Ontario, UWA–1 from Bancroft, Slyudyanka from Lake Baikal, Mud Tank from Australia, McClure Mountain from Colorado, and SDG from Inner Mongolia (China). The relationship between the SiO_2, FeO, and MnO contents in apatite can reflect the origin of the apatite [42], and therefore the apatites from the Moroccan region were plotted against the apatite mentioned by Yang [41] (Figure 7). The Moroccan apatites were thus determined to be of magmatic origin.

The F content of apatites in Morocco ranged from 2.00 wt % to 2.30 wt %, and the Cl content ranged from 0.49 wt % to 0.76 wt % (Table 1). Projecting the F and Cl contents of the samples into the ternary diagram (Figure 8), we found that Moroccan apatites were classified as fluorapatites. However, they had relatively high Cl contents, which indicates that Moroccan apatites are Cl–rich fluorapatites [43]. The F and Cl contents of apatite had a negative correlation (Figure 9), i.e., with the increase in F content, that of Cl decreased. By comparing with apatites of other origins, it was found that the apatites from Morocco had a relatively high Cl content. Since the Cl content in the apatite was directly related to the Cl content in the parent magma, it suggests that the Moroccan magma had a higher Cl content than magma from other regions. Brehler et al. [44] stated that Cl is easily retained in fluids owing to its high solubility in water, making it easy to be removed from the parent rock during differentiation. Conversely, F is not easy to remove. Therefore, the rock mass remelted in the crust often exhibits F-rich and Cl-poor characteristics, which are reflected in the F and Cl compositions of apatite. Comparison with apatites of other origins mentioned by Yang [41] showed that the samples had larger Cl/F ratios (0.21–0.38, Tables 1 and 2), and the mineralised rocks containing such apatites may indicate that the parent magma came

from the subduction zone and the higher Cl/F ratio inherited the halogen composition of the subducted oceanic crust [45,46].

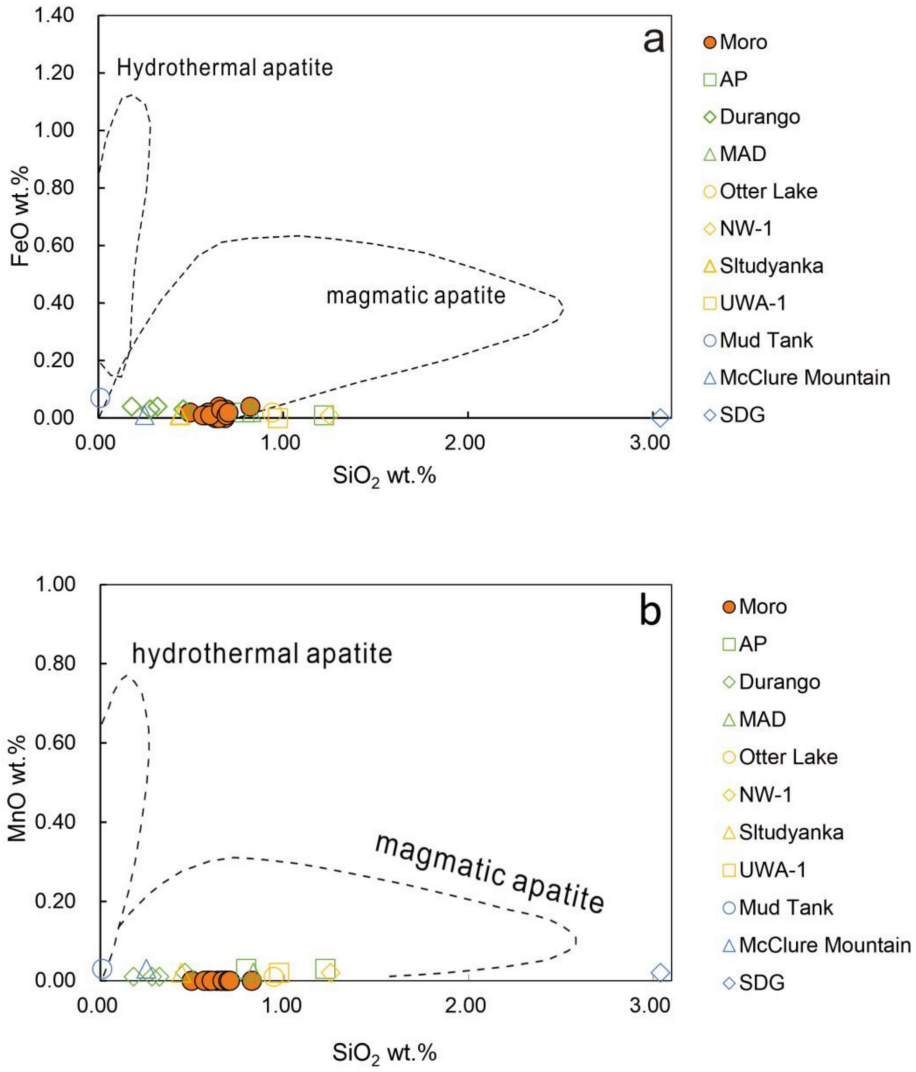

Figure 7. Illustration of the origin of the Moroccan apatites and the apatites mentioned by Yang [41]: (**a**) SiO_2–FeO; (**b**) SiO_2–MnO.

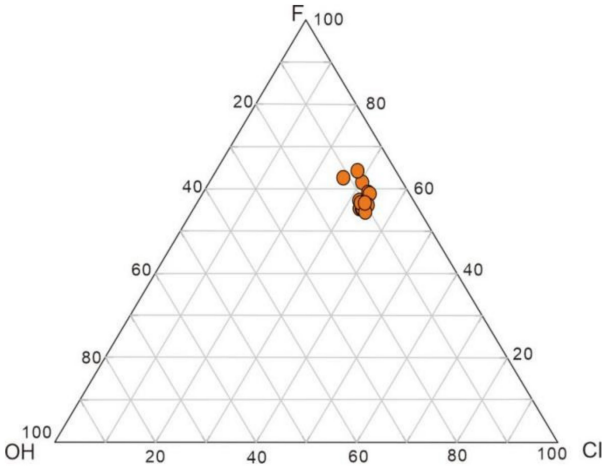

Figure 8. F–Cl–OH ternary diagram of Moroccan apatites.

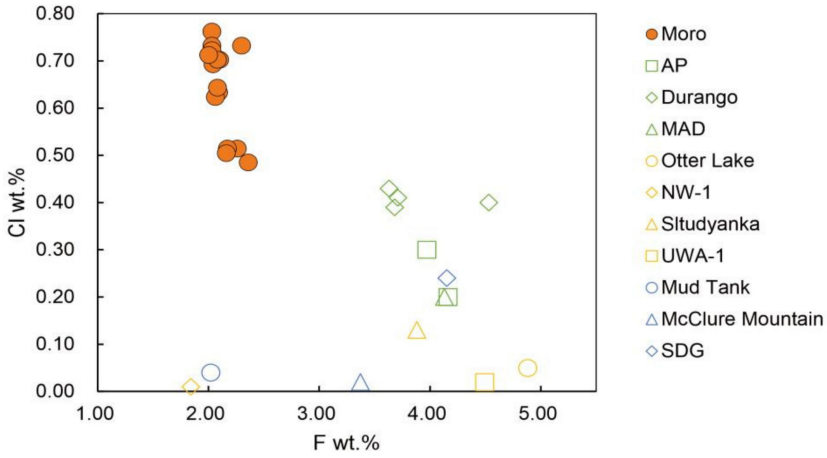

Figure 9. F–Cl diagram of apatites from different origins.

5.2.2. Rare Earth Element Characteristics of Apatite

The trace element data for apatite of different rock types verify that apatite can accommodate a wide range of rare earth elements within its structure, with most elements showing a clear range in concentration and extent (Tables 3 and 4). In the research of Yang [41], we can know that apatite Durango (Mexico) was produced from iron deposits, MAD (Madagascar) from pegmatite, Otter Lake (Canada) from calcite, NW-1 (Ontario) from alkaline carbonatite, Slyudyanka (Lake Baikal) from metamorphic siliciclastic carbonate phosphogypsum, Mud Tank (Austalia) from carbonatite, McClure Mountain (Colorado) from anorthite, and SDG (Inner Mongolia, China) from alkaline ultramafic rocks (AP and NWA-1 generation environment unknown).

The chondrite-normalised REE distribution patterns of apatite usually show negative slopes (high $(Ce/Yb)_N$), indicating relative enrichment in light rare earth elements [3]. The steepest slopes shown in Figure 9 were Mud Tank from carbonate rocks and SDG from ultramafic rocks, which had $(Ce/Yb)_N$ ranging from 113 to 132, whereas the $(Ce/Yb)_N$ values of the other apatites were below 65 (Figure 10). The Moroccan apatite had $(Ce/Yb)_N$ = 31–36, which indicates its low HREE enrichment.

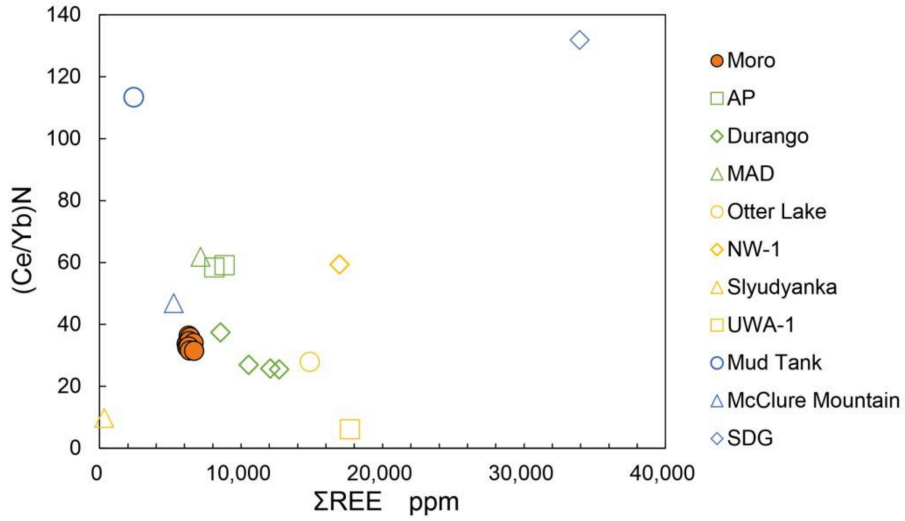

Figure 10. ΣREE–$(Ce/Yb)_N$ of apatites from different origins.

The redox transition from Ce^{3+} to Ce^{4+} or from Eu^{3+} to Eu^{2+} was abnormal in the chondrite standardisation model. Generally speaking, apatite rarely exhibits significant Ce anomalies. Only Mud Tank and Durango showed weak negative Ce anomalies, with δCe values of 0.77 and 0.90–0.93, respectively. In contrast, negative Eu anomalies (Figure 11)

are common in apatite, with Moro-1, AP, MAD, Otter Lake, Slyudyanka, and UWA-1 all showing weak negative Eu anomalies. Durango showed a strong negative Eu anomaly, NW-1 and SDG showed no Eu anomaly, and McClure Mountain showed a strong positive Eu anomaly. In conclusion, the magnitude of the Eu anomaly in apatite increased for larger fractionated rocks and may be constrained by feldspar crystallisation [3,47].

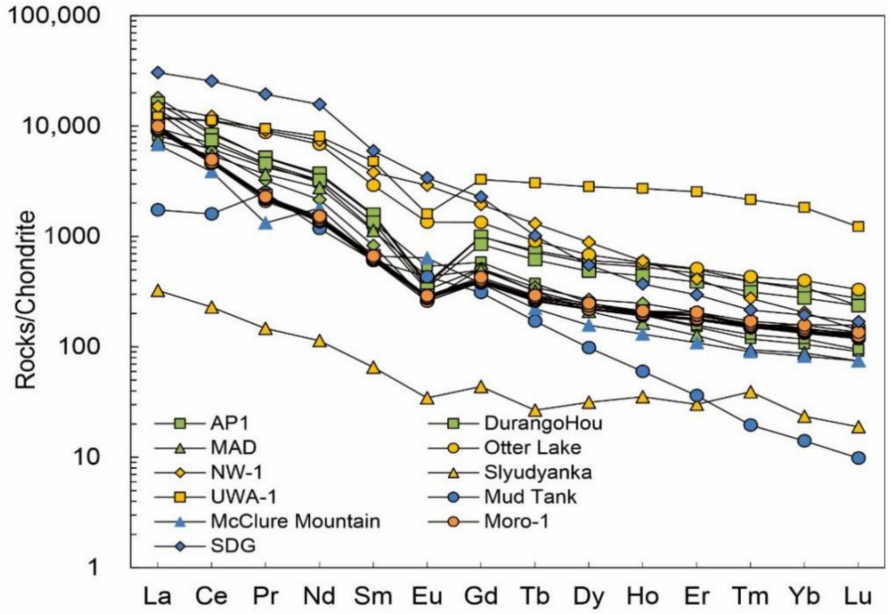

Figure 11. Chondrite-normalised REE distribution patterns of the apatite reference materials analysed in this study. The normalisation values for chondrite are from McDonough and Sun (1989) [40].

In addition, apatite from the Imilchil deposit, also from Central High Atlas, Morocco, was selected to compare the rare earth element characteristics with apatite from the Anemzi deposit (Table 5). Apatite from the Imilchil deposit had a higher rare earth element with ΣREE = 10905.4 ppm [48], while the total rare earth content of the samples was 6152–6674 ppm. Compared to the apatite from Anemzi, the $(Ce/Yb)_N$ (= 13) of the apatite from Imilchil was smaller, which indicated a low enrichment of light rare earth elements in the apatite from Imilchil. Imilchil apatite had an Eu/Eu* value of 0.27, showing a more strongly negative Eu anomaly than the Eu/Eu* (0.53–0.57) value of Anemzi.

5.2.3. Redox Characteristics of Magma

The SO_3 content of apatite in magmatic rocks is indicative of the sulphur content, sulphur escape, and redox state in the melt with which it is in equilibrium, and it is of great significance to magma-related mineralisation [17,49,50]. Sulphur in the melt enters the apatite usually in the form of S^{6+}, and the following two main reactions occur: $S^{6+} + Si^{4+} = 2P^{5+}$ and $S^{6+} + Na^{+} = P^{5+} + Ca^{2+}$. The oxidised magma favours the presence of sulphur in the form of SO_4^{2-}. On the basis of the results of the major element test, the sulphur in the samples was mainly present as S^{6+}, which indicates a high degree of magma oxidation in the Moroccan area. Apatite can be classified by SO_3 content, i.e., high-sulphur apatite if greater than 0.7 wt %, medium-sulphur apatite if 0.3–0.7 wt %, and low-sulphur apatite if less than 0.3 wt % [47,48]. The main factors affecting the SO_3 content of the apatite are the oxygen and sulphur fugacities of the environment system [51]. The sulphur content of the apatite from Morocco ranged from 0.4 to 0.61 wt %, which indicates that the apatite at this site is medium-sulphur apatite. The sulphur content of the apatites in other areas was found to be lower than the detection limit, thus showing that the oxygen and sulphur fugacities of the magma in Morocco are higher than those in other areas.

Mn, Eu, and Ce are elements in variable oxidation states that can be substituted with other elements in apatite. Mn^{2+}, Eu^{3+}, and Ce^{3+} are more accessible in terms of entering

the apatite than Mn^{4+}, Eu^{2+}, and Ce^{4+} because they can replace Ca^{2+} directly or indirectly. Therefore, the oxidation status of the magma can be discerned using the Mn, Eu and Ce contents.

The Mn concentration in the apatite was negatively correlated with magma oxygen fugacity. Miles et al. [52] proposed an empirical formula for calculating magma oxygen fugacity in terms of Mn concentration in apatite: $\lg fO_2 = -0.0022(\pm 0.0003)\,Mn(ppm) - 9.76(\pm 0.46)$. Bringing the Mn concentration of Moro-1 into the equation gives a range of $\lg fO_2$ from −9.95 to −10.00. Overall, the magma in the Moroccan area was found to have a high oxygen fugacity.

The substitution of rare earth elements in the apatite follows the principle of proximity. The smaller the radius difference of the ions, the easier the replacement that occurs. Apatite has a more obvious preference for Eu^{3+} and Ce^{3+} compared with Eu^{2+} and Ce^{4+}. This is because the ionic radius of Ca^{2+} is closer to that of Eu^{3+} compared with Eu^{2+}, whereas the radius of Ce^{3+} is close to that of Ca^{2+} in both seven- and ninefold coordinations [53,54]. Under oxidising conditions, Eu^{2+} and Ce^{3+} are converted into Eu^{3+} and Ce^{4+}, respectively. With the whole-rock composition, temperature, and possible pressure kept constant, low oxygen fugacity results in higher Eu^{2+}/Eu^{3+} and Ce^{3+}/Ce^{4+} ratios as well as lower Eu^{3+} content [10,55]. Therefore, the crystallisation of apatite under low oxygen fugacity will produce a strong negative Eu anomaly [53]. In contrast, the Moroccan apatite showed a weaker negative Eu anomaly, further suggesting a relatively high oxygen fugacity of the magma in the region. However, the variation of individual elements may be controlled by not only the oxidation state of the magma but also other possible factors, such as the segregated crystallisation of feldspar, which may also affect the Eu content of the magma.

Cao et al. [53] showed that $(Eu/Eu^*)_N$ better represents the redox state of the parent magma than $(Ce/Ce^*)_N$. The authors emphasised that the $(Eu/Eu^*)_N$ depth anomaly represents a reducing environment, whereas a $(Eu/Eu^*)_N$ weak-to-moderate anomaly represents a more oxidising environment. On the basis of the work of Cao et al. [53], we plotted the $(Ce/Ce^*)_N$–$(Eu/Eu^*)_N$ diagram for Moroccan apatite (Figure 12), and it was clear that the Moroccan apatite was located in a moderately oxidised magmatic environment. In addition, redox conditions for magmatic apatites of other origins involved in the work of Yang [41] are also shown in Figure 12. The apatites from Madagascar (AP and MAD) are produced from a moderately oxidising environment; the apatite from Mexico (Durango) is produced from a moderately reducing environment; and the apatites from Lake Baikal, Australia, and Colorado are produced from an oxidising environment.

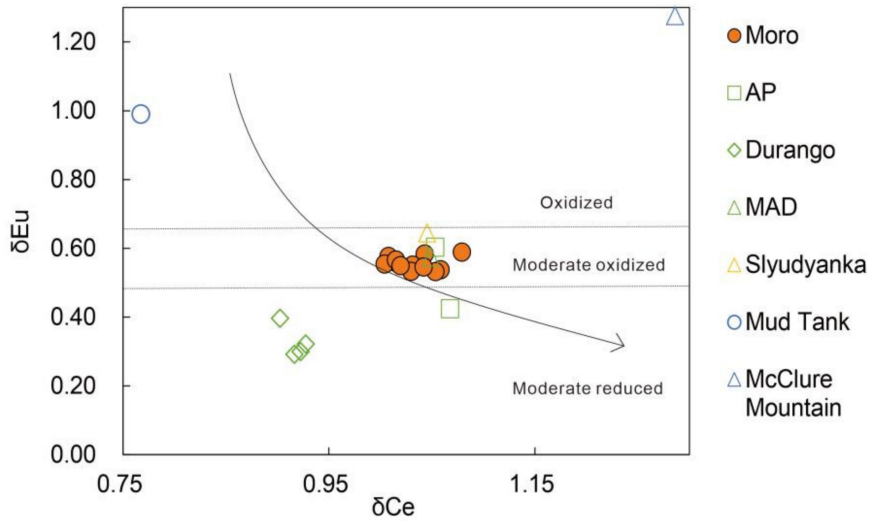

Figure 12. $(Ce/Ce^*)_N$–$(Eu/Eu^*)_N$ diagram of the magmatic apatite, reflecting the degree of magma redox and oxygen escape [53] [δCe = $(Ce/Ce^*)_N$ and δEu = $(Eu/Eu^*)_N$]. Modified from Cao et al. [53].

6. Conclusions

The igneous apatite produced in Morocco has good scientific value and has the potential to become a standard sample. Through gemmological and spectroscopic tests on the Moroccan apatites, the Moroccan apatites were identified as fluorapatites. At the same time, the test results of the major and trace elements also showed that the Moroccan apatites contained high F and relatively low Cl contents, which are characteristic of Cl-rich fluorapatite.

Compared with apatites from other origins (Mexico, Madagascar, Canada, Ontario, Bancrof, Lake Baikal, Australia, Colorado, Inner Mongolia), the Cl content in the Moroccan apatites is relatively high, which is due to the higher Cl content in the parent magma. The SO_3 content of the Moroccan apatites reach the standard of medium-sulphur apatites, which indicates the high oxygen and sulphur fugacities of the magma in the region. In addition, according to the weak negative Eu anomaly of the samples and the $(Ce/Ce^*)_N$–$(Eu/Eu^*)_N$ diagram, it can be confirmed that the oxidation degree of the magma is high.

Author Contributions: Writing—original draft, P.Y.; writing—review and editing, P.Y., B.X. and Z.W.; investigation, P.Y. and D.L.; data curation, P.Y., B.X.; software, P.Y.; methodology, B.X.; resources, B.X. All authors have read and agreed to the published version of the manuscript.

Funding: This research was funded by National Key Technologies R&D Program, 2019YFA0708602, 2020YFA0714802, National Natural Science Foundation of China (42073038, 41803045), Young Talent Support Project of CAST, the Fundamental Research Funds for the Central Universities (Grant no. 265QZ2021012), and IGCP-662.

Data Availability Statement: The data presented in this study are available within the article.

Acknowledgments: This is the fourth contribution of B.X. for National Mineral Rock and Fossil Specimens Resource Center. We thank reviewers for constructive comments which helped in improving our paper.

Conflicts of Interest: The authors declare no conflict of interest.

Appendix A

Table 1. Chemical composition and structural formula of Moroccan apatite, analysed by EMPA (in wt %).

	Moro-1-1	**Moro-1-2**	**Moro-1-3**	**Moro-1-4**	**Moro-1-5**	**Moro-1-6**	**Moro-1-7**	**Moro-1-8**	**Moro-2-1**	**Moro-2-2**	**Moro-2-3**	**Moro-2-4**	**Moro-2-5**	**Moro-2-6**	**Moro-2-7**	**Moro-2-8**
CaO	54.10	54.55	54.48	53.98	54.21	54.25	54.39	54.31	54.43	54.45	54.41	54.49	54.55	54.32	54.40	54.24
P_2O_5	39.63	39.58	40.06	39.76	40.11	39.97	40.02	39.95	40.24	40.48	40.62	40.41	40.59	39.47	39.84	39.85
SO_3	0.53	0.60	0.40	0.53	0.48	0.40	0.44	0.44	0.47	0.40	0.45	0.43	0.41	0.49	0.47	0.46
SiO_2	0.67	0.82	0.50	0.63	0.68	0.65	0.65	0.69	0.68	0.59	0.58	0.56	0.60	0.66	0.69	0.70
Na_2O	0.06	0.08	0.08	0.07	0.07	0.05	0.03	0.00	0.09	0.09	0.05	0.06	0.05	0.07	0.06	0.07
FeO	0.02	0.04	0.02	0.00	0.00	0.04	0.00	0.03	0.02	0.02	0.01	0.01	0.01	0.03	0.01	0.02
MnO	0.00	0.00	0.00	0.00	0.00	0.00	0.00	0.00	0.00	0.00	0.00	0.00	0.00	0.00	0.00	0.00
SrO	0.03	0.08	0.05	0.01	0.00	0.00	0.03	0.00	0.10	0.05	0.08	0.06	0.05	0.09	0.00	0.07
Ce_2O_3	0.27	0.31	0.24	0.24	0.31	0.30	0.37	0.18	0.34	0.33	0.24	0.31	0.30	0.27	0.27	0.29
As_2O_3	0.00	0.05	0.03	0.03	0.01	0.01	0.03	0.04	0.00	0.06	0.03	0.00	0.04	0.04	0.03	0.00
F	2.04	2.10	2.26	2.30	2.09	2.17	2.16	2.36	2.03	2.03	2.04	2.03	2.06	2.08	2.00	2.08
Cl	0.71	0.70	0.51	0.73	0.63	0.51	0.50	0.49	0.76	0.73	0.69	0.72	0.62	0.70	0.71	0.64
Total	97.69	98.44	98.42	97.86	98.20	98.07	98.31	98.37	98.76	98.83	98.86	98.66	98.99	97.87	98.07	97.77
Cl/F	0.35	0.33	0.23	0.32	0.30	0.24	0.23	0.21	0.38	0.36	0.34	0.36	0.30	0.34	0.36	0.31
Cations(apfu)																
Si^{4+}	0.055	0.067	0.040	0.052	0.056	0.053	0.053	0.057	0.055	0.048	0.047	0.046	0.049	0.054	0.056	0.057
Ca^{2+}	4.736	4.753	4.769	4.721	4.720	4.752	4.758	4.763	4.701	4.697	4.695	4.708	4.713	4.681	4.717	4.688
Na^{+}	0.010	0.013	0.013	0.011	0.011	0.008	0.005	0.000	0.014	0.014	0.008	0.009	0.008	0.011	0.009	0.011
Fe^{2+}	0.001	0.001	0.001	0.000	0.000	0.003	0.000	0.002	0.001	0.001	0.001	0.001	0.001	0.002	0.001	0.001
Mn^{2+}	0.000	0.000	0.000	0.000	0.000	0.000	0.000	0.000	0.001	0.001	0.000	0.000	0.001	0.000	0.000	0.000
Ce^{2+}	0.008	0.009	0.007	0.007	0.009	0.009	0.011	0.005	0.010	0.010	0.007	0.009	0.009	0.008	0.008	0.009
P^{5+}	2.741	2.725	2.771	2.747	2.760	2.766	2.766	2.768	2.747	2.759	2.770	2.759	2.771	2.704	2.746	2.738
F^{-}	0.184	0.181	0.133	0.189	0.163	0.133	0.130	0.126	0.194	0.187	0.177	0.184	0.159	0.180	0.184	0.165
Cl^{-}	0.099	0.097	0.071	0.101	0.087	0.071	0.070	0.067	0.104	0.100	0.095	0.099	0.085	0.096	0.098	0.089

Table 2. Chemical composition and structural formula of apatite from other origins, analysed by EMPA (in wt %). Data derived from [41].

	AP1	AP2	DurangoChew	Durango Fishier	DurangoGriffin	Durango Hou	MAD	Otter Lake	NW-1	Sltudyanka	UWA-1	Mud Tank	McClure Mountain	SDG
CaO	55.57	55.66	53.9	53.99	53.85	53.94	55.3	53.44	54.24	54.66	53.67	55.3	55.08	51.58
P_2O_5	40.82	39.74	41.88	42.16	41.91	42.25	39.94	38.45	39.81	40.7	40.12	42.09	41.83	34.48
SiO_2	0.79	1.22	0.46	0.18	0.32	0.28	0.83	0.94	1.25	0.44	0.97	0.01	0.25	3.04
FeO	0.02	0.01	0.03	0.04	0.04	0.03	0.02	0.02	0.01	0.01	bdl	0.07	0.01	bdl
MnO	0.03	0.03	0.02	0.01	0.01	0.01	0.02	0.01	0.02	0.02	0.02	0.03	0.03	0.02
MgO	bdl	0.01	0.04	0.02	0.02	0.03	0.01	bdl	0.01	0.01	0.01	0.06	0.01	0.01
SrO	0.24	0.07	0.05	0.04	0.05	0.05	0.17	0.2	0.53	0.14	0.1	0.35	0.4	1.44
Cl	0.3	0.2	0.41	0.43	0.4	0.39	0.2	0.05	0.01	0.13	0.02	0.04	0.02	0.24
F	3.97	4.16	3.71	3.63	4.53	3.68	4.13	4.88	1.84	3.88	4.49	2.02	3.37	4.15
Total	100.01	99.3	99.21	99.44	99.54	99.44	98.83	96.58	96.96	99.58	97.42	99.33	99.59	93.21
Cl/F	0.08	0.05	0.11	0.12	0.09	0.11	0.05	0.01	0.01	0.03	0.004	0.02	0.01	0.06
Cations (apfu)														
Ca^{2+}	4.846	4.943	4.667	4.651	4.665	4.648	4.910	4.946	4.895	4.834	4.841	4.781	4.795	4.846
Fe^{2+}	0.001	0.000	0.002	0.003	0.003	0.002	0.001	0.001	0.001	0.001	0.000	0.005	0.001	0.001
Mn^{2+}	0.001	0.001	0.001	0.001	0.001	0.001	0.001	0.001	0.001	0.001	0.001	0.002	0.002	0.001
P^{5+}	2.813	2.789	2.865	2.870	2.869	2.877	2.802	2.812	2.839	2.844	2.859	2.876	2.877	2.813
Mg^{2+}	0.000	0.001	0.005	0.002	0.002	0.004	0.001	0.000	0.001	0.001	0.001	0.007	0.001	0.000
F^-	0.077	0.052	0.105	0.109	0.102	0.099	0.052	0.014	0.003	0.034	0.005	0.010	0.005	0.077
Cl^-	0.041	0.028	0.056	0.059	0.055	0.053	0.028	0.007	0.001	0.018	0.003	0.005	0.003	0.041

bdl = below detection limit.

Table 3. Chemical composition and structural formula of Moroccan apatite, analysed by LA-ICP-MS.

		Moro-1-1	**Moro-1-2**	**Moro-1-3**	**Moro-1-4**	**Moro-1-5**	**Moro-1-6**	**Moro-1-7**	**Moro-1-8**	**Moro-1-9**	**Moro-1-10**	**Moro-1-11**	**Moro-1-12**
Ti	ppm	0.59	0.39	0.60	0.43	0.00	0.04	0.17	0.82	0.39	0.33	0.36	0.17
Mn	ppm	107.57	107.82	101.21	102.40	89.11	96.17	86.79	98.98	91.11	93.90	94.17	96.31
Rb	ppm	0.12	0.00	0.00	0.02	0.00	0.00	0.00	0.00	0.01	0.10	0.00	0.00
Sr	ppm	618.13	650.80	623.41	616.86	621.01	629.42	610.33	636.82	628.45	638.76	647.13	645.73
ZrO_2	wt%	0.00	0.00	0.00	0.00	0.00	0.00	0.00	0.00	0.00	0.00	0.00	0.00
Nb	ppm	0.01	0.02	0.02	0.01	0.02	0.02	0.02	0.01	0.01	0.03	0.02	0.03
Ba	ppm	1.29	1.21	1.25	1.53	1.31	1.27	1.32	1.62	1.34	1.34	1.31	1.30
La	ppm	2117.01	2128.08	2189.76	2206.03	2097.55	2193.51	2257.56	2328.49	2168.07	2177.43	2217.85	2304.67
Ce	ppm	2763.91	2886.02	2784.85	2881.89	2805.83	2851.43	2939.25	2954.81	2746.28	2797.01	2817.56	2976.57
Pr	ppm	193.71	202.07	209.67	208.12	203.39	209.55	216.96	218.62	207.44	209.65	207.02	212.87
Nd	ppm	639.77	632.75	635.55	649.15	621.02	635.10	663.70	664.60	635.88	643.40	670.83	696.82
Sm	ppm	90.72	90.72	91.95	94.27	91.13	94.51	96.99	100.26	93.16	96.10	95.95	99.82
Eu	ppm	14.78	16.02	15.91	16.51	14.71	15.73	15.55	16.63	15.59	16.45	15.95	16.55
Gd	ppm	77.45	75.99	77.15	79.04	78.10	80.34	81.74	82.53	79.06	82.02	81.73	85.78
Tb	ppm	9.68	9.50	9.78	9.76	9.65	9.81	10.09	10.45	9.76	10.06	10.36	10.72
Dy	ppm	55.94	54.30	54.42	55.37	54.32	55.27	58.10	58.80	54.57	58.15	58.43	61.60
Ho	ppm	10.67	10.60	10.79	10.72	10.70	11.06	11.29	11.68	10.92	11.03	11.60	11.71
Er	ppm	28.34	28.43	28.37	28.53	28.39	29.30	31.15	31.83	29.35	31.09	31.44	33.27
Tm	ppm	3.78	3.77	3.72	3.83	3.79	3.87	3.97	4.05	3.90	3.91	4.07	4.26
Yb	ppm	22.79	22.02	22.83	22.32	22.95	22.87	24.42	24.09	23.38	23.66	24.78	26.22
Lu	ppm	2.99	2.95	2.97	3.02	3.04	3.18	3.24	3.32	3.15	3.10	3.12	3.38
Hf	ppm	0.01	0.01	0.02	0.00	0.01	0.01	0.00	0.00	0.01	0.00	0.00	0.02
Ta	ppm	0.00	0.00	0.00	0.00	0.00	0.00	0.00	0.00	0.00	0.00	0.00	0.00
Pb	ppm	1.62	1.67	1.66	1.80	1.60	1.69	1.65	1.81	1.69	1.70	1.69	1.75

Table 3. *Cont.*

		Moro-1-1	Moro-1-2	Moro-1-3	Moro-1-4	Moro-1-5	Moro-1-6	Moro-1-7	Moro-1-8	Moro-1-9	Moro-1-10	Moro-1-11	Moro-1-12
Th	ppm	184.37	181.57	183.30	188.67	181.81	190.45	193.79	201.34	192.29	195.07	196.11	204.33
U	ppm	16.48	17.18	18.09	18.91	16.24	17.33	17.31	17.88	17.20	17.27	17.52	18.08
ΣLREE	ppm	5819.89	5955.67	5927.67	6055.97	5833.63	5999.83	6190.02	6283.41	5866.43	5940.04	6025.15	6307.31
ΣHREE	ppm	211.65	207.57	210.02	212.60	210.94	215.69	224.00	226.73	214.09	223.01	225.54	236.96
ΣREE	ppm	6031.54	6163.24	6137.69	6268.57	6044.57	6215.52	6414.02	6510.14	6080.52	6163.05	6250.69	6544.27
δEu		0.539	0.590	0.577	0.585	0.533	0.552	0.534	0.559	0.555	0.567	0.551	0.547
δCe		1.058	1.079	1.008	1.043	1.053	1.031	1.030	1.015	1.004	1.015	1.020	1.042

Table 4. Characteristics of apatite from different production areas.

Origin	Color	Luster	Transparency	RI	DR	SG	Uv	Pleochroism	Size	Feature Observation
Durango, Mexico	Homogeneous greenish yellow	glassy lustre	transparent	1.631–1.636	0.005	3.21	inert to long-wave; weak yellow to short-wave	weak dichroism	the largest of which measured 14.97 × 9.47 × 7.97 mm	Emerald- and cushion-cut. The cushion-cut stone revealed straight growth zoning. The emerald-cut contained a small liquid feather.
Ling qiu, Shanxi Province	Yellow, dark green and dark blue-green	glassy lustre	translucent to transparent	1.632–1.639	0.004	3.19—3.22	inert	medium dichroism	the largest of which measured 3 × 1 × 0.5 cm	Hexagonal columnar or subhexagonal columnar crystal form; high degree of self-formation showing massive or columnar.
Anhui Province	light yellow	glassy lustre to weak glassy lustre	transparent	1.633–1.637 1.635—1.638	0.004 0.003	3.19—3.20	medium yellow-green		the largest of which measured 1.5 × 0.4 × 0.5 cm	Sheet-like and plate-like, poorly self-formation, no obvious crystalline shape, obvious longitudinal lines between crystal faces.

Table 4. *Cont.*

Origin	Color	Luster	Transparency	RI	DR	SG	Uv	Pleochroism	Size	Feature Observation
Shaanxi Province	Gray-green	glassy lustre	transparent	1.633–1.637 1.634–1.636	0.004 0.002	2.70–2.71	inert	weak dichroism	the largest of which measured 6.5 × 4 × 4 mm	Massive, with obvious hexagonal columnar crystal form, high degree of self-formation, smooth surface, and poor cleavage.

Table 5. Chemical composition and structural formula of Moroccan apatite, analysed by LA-ICP-MS. Data derived from [41,48].

		AP1	AP2	DurangoChew	Durango Fishier	DurangoGriffin	Durango Hou	MAD	Otter Lake	NW-1	Sltudyanka	UWA-1	Mud Tank	McClure Mountain	SDG	Imilchil
Rb	ppm	0.18	0.26	0.12	0.11	0.13	0.12	0.25	0.43	0.15	0.02	0.44	0.22	0.12	0.2	-
Sr	ppm	2506	591	482	456	491	476	1650	1668	5512	1231	1186	2681	3422	11,368	953
Ba	ppm	1.3	1.5	1.7	1.4	1.8	1.5	1.2	2	13	10	0.8	83	8.3	1.3	0.6
Nb	ppm	0.23	2.6	1	0.02	0.03	0.02	0.07	0.26	4.6	0.43	0.7	0.42	0.15	2.4	-
Ta	ppm	0.01	0.03	0	0	0	0	0.01	0.08	0.07	0	0.85	0.03	0.03	0.03	-
Zr	ppm	5.9	6.3	1.4	0.6	1.1	0.8	9.8	1.61	52	5.79	1.71	1.9	3.2	48	8
Hf	ppm	0.31	0.51	0.23	0.19	0.23	0.26	0.45	0.08	0.24	0.29	0.13	0.1	0.2	0.39	-
Pb	ppm	15	48	0.9	0.4	0.7	0.6	16	61	26	10	56	3	3.7	50	2.7
Th	ppm	647	2095	320	151	270	231	661	753	48	142	828	11	38	705	285
U	ppm	24	66	20	7	11	11	19	99	122	68	165	2.1	12	47	31
La	ppm	1925	2269	4285	3176	3819	3334	1745	2772	3576	77	2857	414	1609	7209	2457
Ce	ppm	3783	4261	5405	3635	5178	4561	3338	6832	7477	140	6876	980	2362	15,668	3708
Pr	ppm	403	422	488	307	496	436	349	832	865	14	901	237	126	1843	303
Nd	ppm	1501	1435	1677	1009	1745	1514	1290	3205	3468	53	3747	550	843	7344	1487
Sm	ppm	205	178	237	127	244	207	173	445	582	10	731	93	102	911	274
Eu	ppm	31	19	21	15	22	20	25	78	169	2	93	25	37	196	35
Gd	ppm	120	105	204	105	206	174	102	275	400	9	676	64	77	468	588

Table 5. *Cont.*

		AP1	AP2	DurangoChew	Durango Fishier	DurangoGriffin	Durango Hou	MAD	Otter Lake	NW-1	Sltudyanka	UWA-1	Mud Tank	McClure Mountain	SDG	Imilchil
Tb	ppm	14	12	28	13	27	23	12	34	49	1	114	6.4	8.3	38	39
Dy	ppm	64	61	154	68	146	123	53	173	225	8	716	25	40	140	245
Ho	ppm	11	11	32	14	30	25	9.2	33	34	2	154	3.4	7.4	21	48
Er	ppm	25	26	83	34	77	64	21	85	68	5	421	6	18	49	129
Tm	ppm	3	3.3	10	4	10	8	2.4	11	7	1	55	0.5	2.3	5.5	16
Yb	ppm	18	20	59	27	56	47	15	68	35	4	311	2.4	14	33	81
Lu	ppm	2.3	2.4	6	4	7	6	1.9	8.4	3.6	0.48	31	0.25	1.9	4.3	8.4
Y	ppm	309	321	911	427	886	762	257	889	851	46	3583	73	206	605	1455
ΣLREE	ppm	7848	8584	12,113	8269	11,504	10,072	6920	14,164	16,137	296	15,205	2299	5079	33,171	8296
ΣHREE	ppm	257.3	240.7	576	269	559	470	216.5	687.4	821.6	30.48	2478	107.95	168.9	758.8	2609.4
ΣREE	ppm	8105.3	8824.7	12,689	8538	12,063	10,542	7136.5	14,851.4	16,958.6	326.48	17,683	2406.95	5247.9	33,929.8	10,905.4
δEu		0.60	0.42	0.29	0.40	0.30	0.32	0.58	0.68	1.07	0.64	0.40	0.99	1.28	0.92	0.27
δCe		1.05	1.07	0.92	0.90	0.92	0.93	1.05	1.10	1.04	1.05	1.05	0.77	1.29	1.05	1.05

References

1. Bruand, E.; Fowler, M.; Storey, C.; Darling, J. Apatite trace element and isotope applications to petrogenesis and provenance. *Am. Mineral.* **2017**, *102*, 75–84. [CrossRef]
2. Boyce, J.W.; Hervig, R.L. Apatite as a Monitor of Late-Stage Magmatic Processes at Volcán Irazú, Costa Rica. *Contrib. Miner. Petrol.* **2009**, *157*, 135–145. [CrossRef]
3. Belousova, E.A.; Griffin, W.L.; O'reilly, S.Y.; Fisher, N.I. Apatite as an indicator mineral for mineral exploration: Trace-element compositions and their relationship to host rock type. *J. Geochem. Explor.* **2002**, *76*, 45–69. [CrossRef]
4. Zhang, F.; Li, W.; White, N.; Zhang, L.; Qiao, X.; Yao, Z. Geochemical and isotopic study of metasomatic apatite: Implications for gold mineralization in Xindigou, northern China. *Ore Geol. Rev.* **2020**, *127*, 103853. [CrossRef]
5. Ren, Z.; Cui, J.; Liu, C.; Li, T.; Chen, G.; Dou, S.; Tian, T.; Luo, Y. Apatite Fission Track Evidence of Uplift Cooling in the Qiangtang Basin and Constraints on the Tibetan Plateau Uplift. *Acta Geol. Sin. Engl. Ed.* **2015**, *89*, 467–484. [CrossRef]
6. Ouabid, M.; Raji, O.; Dautria, J.; Bodinier, J.; Parat, F.; El Messbahi, H.; Garrido, C.; Ahechach, Y. Petrological and geochemical constraints on the origin of apatite ores from Mesozoic alkaline intrusive complexes, Central High-Atlas, Morocco. *Ore Geol. Rev.* **2021**, *136*, 104250. [CrossRef]
7. Pasero, M.; Kampf, A.R.; Ferraris, C.; Pekov, I.V.; Rakovan, J.; White, T.J. Nomenclature of the Apatite Supergroup Minerals. *Eur. J. Mineral.* **2010**, *22*, 163–179. [CrossRef]
8. Rossi, M.; Ghiara, M.R.; Chita, G.; Capitelli, F. Crystal-Chemical and Structural Characterization of Fluorapatites in Ejecta from Somma-Vesuvius Volcanic Complex. *Am. Mineral.* **2011**, *96*, 1828–1837. [CrossRef]
9. Pan, Y.; Fleet, M.E. Compositions of the Apatite-Group Minerals: Substitution Mechanisms and Controlling Factors. *Rev. Mineral. Geochem.* **2002**, *48*, 13–49. [CrossRef]
10. Sha, L.-K.; Chappell, B.W. Apatite Chemical Composition, Determined by Electron Microprobe and Laser-Ablation Inductively Coupled Plasma Mass Spectrometry, as a Probe into Granite Petrogenesis. *Geochim. Cosmochim. Acta* **1999**, *63*, 3861–3881. [CrossRef]
11. Xu, B.; Hou, Z.-Q.; Griffin, W.L.; Lu, Y.; Belousova, E.; Xu, J.-F.; O'Reilly, S.Y. Recycled Volatiles Determine Fertility of Porphyry Deposits in Collisional Settings. *Am. Mineral.* **2021**, *106*, 656–661. [CrossRef]
12. Chen, N.; Pan, Y.; Weil, J.A. Electron Paramagnetic Resonance Spectroscopic Study of Synthetic Fluorapatite: Part I. Local Structural Environment and Substitution Mechanism of Gd^{3+} at the Ca2 Site. *Am. Mineral.* **2002**, *87*, 37–46. [CrossRef]
13. Fleet, M.E.; Pan, Y. Site Preference of Rare Earth Elements in Fluorapatite. *Am. Mineral.* **1995**, *80*, 329–335. [CrossRef]
14. Mao, M.; Rukhlov, A.S.; Rowins, S.M.; Spence, J.; Coogan, L.A. Apatite Trace Element Compositions: A Robust New Tool for Mineral Exploration. *Econ. Geol.* **2016**, *111*, 1187–1222. [CrossRef]
15. Rakovan, J.F.; Hughes, J.M. Strontium in the apatite structure: Strontium fluorapatite and belovite–(Ce). *Can. Mineral.* **2000**, *38*, 839–845. [CrossRef]
16. Piccoli, P.M.; Candela, P.A. Apatite in Igneous Systems. *Rev. Mineral. Geochem.* **2002**, *48*, 255–292. [CrossRef]
17. Hughes, J.M.; Ertl, A.; Bernhardt, H.-J.; Rossman, G.R.; Rakovan, J. Mn-Rich Fluorapatite from Austria: Crystal Structure, Chemical Analysis, and Spectroscopic Investigations. *Am. Mineral.* **2004**, *89*, 629–632. [CrossRef]
18. Sudarsanan, K.; Young, R.A.; Wilson, A.J.C. The Structures of Some Cadmium 'apatites' $Cd_5(MO_4)_3X$. I. Determination of the Structures of $Cd_5(VO_4)_3I$, $Cd_5(PO_4)_3Br$, $Cd_3(AsO_4)_3Br$ and $Cd_5(VO_4)_3Br$. *Acta Cryst. B Struct. Sci.* **1977**, *33*, 3136–3142. [CrossRef]
19. Peng, G.; Luhr, J.F.; McGee, J.J. Factors Controlling Sulfur Concentrations in Volcanic Apatite. *Am. Mineral.* **1997**, *82*, 1210–1224. [CrossRef]
20. Perseil, E.-A.; Blanc, P.; Ohnenstetter, D. As-Bearing Fluorapatite in Manganiferous Deposits from St. Marcel - Praborna, Val D'Aosta, Italy. *Can. Mineral.* **2000**, *38*, 101–117. [CrossRef]
21. Xu, B.; Hou, Z.-Q.; Griffin, W.L.; Zheng, Y.-C.; Wang, T.; Guo, Z.; Hou, J.; Santosh, M.; O'Reilly, S.Y. Cenozoic Lithospheric Architecture and Metallogenesis in Southeastern Tibet. *Earth-Sci. Rev.* **2021**, *214*, 103472. [CrossRef]
22. Michard, A.; Cailleux, Y.; Hoepfffner, C. L'orogénese mésétien du Maroc: Structure, deformation hercynienne et déplacements. *Mém. Serv. Géol. Maroc* **1989**, *335*, 313–327.
23. Choubert, G. Histoire geologique du Precambrien de l'Anti-Atlas. *Notes Mem. Serv. Geol. Maroc* **1963**, *162*, 352.
24. Ghorbal, B.; Bertotti, G.; Foeken, J.; Andriessen, P. Unexpected Jurassic to Neogene Vertical Movements in 'Stable' Parts of NW Africa Revealed by Low Temperature Geochronology. *Terra Nova* **2008**, *20*, 355–363. [CrossRef]
25. Oukassou, M.; Saddiqi, O.; Barbarand, J.; Sebti, S.; Baidder, L.; Michard, A. Post-Variscan Exhumation of the Central Anti-Atlas (Morocco) Constrained by Zircon and Apatite Fission-Track Thermochronology. *Terra Nova* **2013**, *25*, 151–159. [CrossRef]
26. Xu, B.; Hou, Z.; Zheng, Y.; Zhou, Y.; Zhou, L.; Yang, Y.; Han, Y.; Zhen, G.; Wu, C. Jurassic Hornblende Gabbros in Dongga, Eastern Gangdese, Tibet: Partial Melting of Mantle Wedge and Implications for Crustal Growth. *Acta Geol. Sin. Engl. Ed.* **2017**, *91*, 545–564. [CrossRef]
27. Teixell, A.; Arboleya, M.-L.; Julivert, M.; Charroud, M. Tectonic Shortening and Topography in the Central High Atlas (Morocco): Tectonic Shortening in Morocco. *Tectonics* **2003**, *22*, 1051. [CrossRef]
28. Domènech, M.; Teixell, A.; Babault, J.; Arboleya, M.-L. The Inverted Triassic Rift of the Marrakech High Atlas: A Reappraisal of Basin Geometries and Faulting Histories. *Tectonophysics* **2015**, *663*, 177–191. [CrossRef]
29. Piqué, A.; Tricart, P.; Guiraud, R.; Laville, E.; Bouaziz, S.; Amrhar, M.; Ouali, R.A. The Mesozoic-Cenozoic Atlas Belt (North Africa): An Overview. *Geodin. Acta* **2002**, *15*, 185–208. [CrossRef]

30. Laville, E.; Pique, A.; Amrhar, M.; Charroud, M. A Restatement of the Mesozoic Atlasic Rifting (Morocco). *J. Afr. Earth Sci.* **2004**, *38*, 145–153. [CrossRef]
31. Gouiza, M.; Bertotti, G.; Hafid, M.; Cloetingh, S. Kinematic and Thermal Evolution of the Moroccan Rifted Continental Margin: Doukkala-High Atlas Transect: Doukkala-HIGH Atlas Passive Margin. *Tectonics* **2010**, *29*, TC5008. [CrossRef]
32. Michard, A.; Ibouh, H.; Charriere, A. Syncline-topped anticlinal ridges from the high Atlas: A moroccan conundrum, and inspiring structures from the syrian arc, Israel. *Terra Nova* **2011**, *23*, 314–323. [CrossRef]
33. Liu, Y. Mineral Spectroscopy of Apatite. Ph.D. Thesis, Sun Yat-Sen University, Guangzhou, China, 2003.
34. Xu, B.; Kou, G.; Etschmann, B.; Liu, D.; Brugger, J. Spectroscopic, Raman, EMPA, Micro-XRF and Micro-XANES Analyses of Sulphur Concentration and Oxidation State of Natural Apatite Crystals. *Crystals* **2020**, *10*, 1032. [CrossRef]
35. Zolotarev, V.M. Optical Constants of an Apatite Single Crystal in the IR Range of 6–28 Mm. *Opt. Spectrosc.* **2018**, *124*, 262–272. [CrossRef]
36. Li, W. Gemological and chromatographic characterization of blue-green apatite. Master's Thesis, China University of Geosciences, Beijing, China, 2021.
37. Chindudsadeegul, P.; Jamkratoke, M. Effect of Heat Treatment on the Luminescence Properties of Natural Apatite. *Spectrochim. Acta Part A Mol. Biomol. Spectrosc.* **2018**, *204*, 276–280. [CrossRef]
38. Chen, C.-Y.; Huang, W.-Z.; Shao, T.; Li, Z.-B.; Shen, X.-T. Characteristics of Visible Spectrum of Apatite with Alexandrite Effect. *Spectrosc. Spectr. Anal.* **2021**, *41*, 1483–1486.
39. Bačík, P.; Fridrichová, J.; Štubňa, J.; Bancík, T.; Illášová, Ľ.; Pálková, H.; Škoda, R.; Mikuš, T.; Milovská, S.; Vaculovič, T.; et al. The REE-Induced Absorption and Luminescence in Yellow Gem-Quality Durango-Type Hydroxylapatite from Muránska Dlhá Lúka, Slovakia. *Minerals* **2020**, *10*, 1001. [CrossRef]
40. Sun, S.-S.; McDonough, W.F. Chemical and Isotopic Systematics of Oceanic Basalts: Implications for Mantle Composition and Processes. *Geol. Soc. Lond. Spec. Publ.* **1989**, *42*, 313–345. [CrossRef]
41. Yang, Y.-H.; Wu, F.-Y.; Yang, J.-H.; Chew, D.M.; Xie, L.-W.; Chu, Z.-Y.; Zhang, Y.-B.; Huang, C. Sr and Nd Isotopic Compositions of Apatite Reference Materials Used in U–Th–Pb Geochronology. *Chem. Geol.* **2014**, *385*, 35–55. [CrossRef]
42. Liu, J.-W. Characterization of Granitic Apatite Speciation in Jiu Dong and Xiao Qin Ling and its Geological Significance. Master's Thesis, China University of Geosciences, Beijing, China, 2019.
43. Hughes, J.M.; Heffernan, K.M.; Goldoff, B.; Nekvasil, H. CL-Rich Fluorapatite, Devoid of OH, from the Three Peaks Area, Utah: The First Reported Structure of Natural CL-Rich Fluorapatite. *Can. Mineral.* **2014**, *52*, 643–652. [CrossRef]
44. Brehler, B.; Fuge, R. Chlorine. In *Handbook of Geochemistry*; Springer: Berlin, Germany, 1974; Volume 2, pp. 17A–17O.
45. Xing, K.; Shu, Q.-H. Application of apatite in the study of mineralogy. *Miner. Depos.* **2021**, *40*, 189–205. [CrossRef]
46. Xu, B.; Griffin, W.L.; Xiong, Q.; Hou, Z.-Q.; O'Reilly, S.Y.; Guo, Z.; Pearson, N.J.; Gréau, Y.; Yang, Z.-M.; Zheng, Y.-C. Ultrapotassic Rocks and Xenoliths from South Tibet: Contrasting Styles of Interaction between Lithospheric Mantle and Asthenosphere during Continental Collision. *Geology* **2017**, *45*, 51–54. [CrossRef]
47. Van Hoose, A.E.; Streck, M.J.; Pallister, J.S. Apatite sulfur systematics and crystal population in the 1991 Pinatubo magmas. *Chem. Commun.* **2010**, *46*, 6084.
48. Apen, F.E.; Wall, C.J.; Cottle, J.M.; Schmitz, M.D.; Kylander-Clark, A.R.C.; Seward, G.G.E. Apatites for Destruction: Reference Apatites from Morocco and Brazil for U-Pb Petrochronology and Nd and Sr Isotope Geochemistry. *Chem. Geol.* **2022**, *590*, 120689. [CrossRef]
49. Parat, F.; Holtz, F. Sulfur Partition Coefficient between Apatite and Rhyolite: The Role of Bulk S Content. *Contrib. Mineral. Petrol.* **2005**, *150*, 643–651. [CrossRef]
50. Parat, F.; Holtz, F.; Klügel, A. S-Rich Apatite-Hosted Glass Inclusions in Xenoliths from La Palma: Constraints on the Volatile Partitioning in Evolved Alkaline Magmas. *Contrib. Mineral. Petrol.* **2011**, *162*, 463–478. [CrossRef]
51. Yao, C.; Lu, J.; Guo, W. Characterization of apatite generations and composition of porphyry copper ore from Copper Factory, Jiangxi Province. *J. Mineral.* **2007**, *1*, 31–40. [CrossRef]
52. Miles, A.J.; Graham, C.M.; Hawkesworth, C.J.; Gillespie, M.R.; Hinton, R.W.; Bromiley, G.D. Apatite: A New Redox Proxy for Silicic Magmas? *Geochim. Cosmochim. Acta* **2014**, *132*, 101–119. [CrossRef]
53. Cao, M.; Li, G.; Qin, K.; Seitmuratova, E.Y.; Liu, Y. Major and Trace Element Characteristics of Apatites in Granitoids from Central Kazakhstan: Implications for Petrogenesis and Mineralization: Major and Trace Element of Apatites. *Resour. Geol.* **2012**, *62*, 63–83. [CrossRef]
54. Chen, L.; Zhang, Y. In Situ Major-, Trace-Elements and Sr-Nd Isotopic Compositions of Apatite from the Luming Porphyry Mo Deposit, NE China: Constraints on the Petrogenetic-Metallogenic Features. *Ore Geol. Rev.* **2018**, *94*, 93–103. [CrossRef]
55. Xu, B.; Hou, Z.-Q.; Zheng, Y.-C.; Wang, R.; He, M.-Y.; Zhou, L.-M.; Wang, Z.-X.; He, W.-Y.; Zhou, Y.; Yang, Y. In Situ Elemental and Isotopic Study of Diorite Intrusions: Implication for Jurassic Arc Magmatism and Porphyry Cu-Au Mineralisation in Southern Tibet. *Ore Geol. Rev.* **2017**, *90*, 1063–1077. [CrossRef]